The Astrophysical Journal, 890:109 (12pp), 2020 February 20 https://doi.org/10.3847/1538-4357/ab67b3

Standing MHD Waves in a Magnetic Slab Embedded in an Asymmetric Plasma Environment: Slow Surface Waves

William Oxley[1], Noémi Kinga Zsámberger[1,2,3], and Róbert Erdélyi[1,4]
[1] Solar Physics and Space Plasma Research Centre, School of Mathematics and Statistics, University of Sheffield, Hicks Building, Hounsfield Road Sheffield, S3 7RH, UK; robertus@sheffield.ac.uk
[2] Department of Physics, University of Debrecen, Egyetem tér 1., Debrecen, H-4010, Hungary
[3] Doctoral School of Physics, University of Debrecen, Egyetem tér 1., Debrecen, H-4010, Hungary
[4] Department of Astronomy, Eötvös Loránd University, 1/A Pázmány Péter sétány, H-1117, Budapest, Hungary
Received 2019 September 11; revised 2019 December 10; accepted 2020 January 2; published 2020 February 18

Abstract

The field of solar magnetoseismology (SMS) is heavily reliant upon our understanding of magnetohydrodynamic (MHD) waves that occur in many solar features. Building on previous studies of propagating MHD waves in a magnetic slab embedded in a nonmagnetic asymmetric environment, in this study we assume a line-tying boundary condition and use analytical techniques to derive the dispersion relation for linear standing MHD oscillations. The slab is first assumed thin, with arbitrary asymmetry, in order to derive the frequencies of the standing harmonic modes for both slow quasi-sausage and slow quasi-kink waves. Besides this, the asymmetry is assumed to be weak in order to determine the frequency dependence on the width of the slab and the asymmetry of the system, to leading order. For both the quasi-sausage and quasi-kink modes, the derived eigenfrequencies show that the dependence on the asymmetry in the system is much weaker than the dependence on the width of the slab. Using the eigenfrequencies, other observable quantities are derived (such as, e.g., the frequency ratio) providing an opportunity to use SMS to infer background diagnostics of the system.

Unified Astronomy Thesaurus concepts: The Sun (1693); Magnetic fields (994); Magnetohydrodynamics (1964); Solar physics (1476); Solar magnetic fields (1503); Solar oscillations (1515); Solar atmosphere (1477); Solar prominences (1519)

Supporting material: animations

1. Introduction

Observations by high-resolution space-borne satellites and ground-based telescopes enabled the detection of waves and oscillations at multiple wavelengths in a wide range of solar magnetic structures in the Sun's atmosphere, e.g., at large scales including coronal loops (Aschwanden et al. 1999; Wang 2004; Banerjee et al. 2007; de Moortel 2009), plumes (Ofman et al. 1997; DeForest & Gurman 1998; Nakariakov 2006), prominences (Arregui et al. 2012), or small scales, including spicules (Zaqarashvili & Erdélyi 2009; Tsiropoula et al. 2012), pores (Keys et al. 2018), sunspot light bridges (Yuan et al. 2014; Yang et al. 2016, 2017), or magnetic bright points (MBPs; Liu et al. 2018). Magnetohydrodynamic (MHD) waves and oscillations provide us with a tool to diagnose these structures, a method known as solar magnetoseismology (SMS; see reviews by Nakariakov & Verwichte 2005; Erdélyi 2006a, 2006b; Andries et al. 2009; Ruderman & Erdélyi 2009). High-resolution observations of waves and oscillations in magnetic structures, combined with theoretical MHD wave modeling, enable us to determine solar atmospheric parameters that are difficult to measure directly, such as the magnetic field strength (Nakariakov & Ofman 2001; Erdélyi & Taroyan 2008). The principles of SMS were first suggested by Uchida (1970), Zajtsev & Stepanov (1975), and Roberts et al. (1984) in the coronal context, and by Tandberg-Hanssen (1995) for prominence application.

The study of systems similar to the one we will consider here first began with wave propagation at a single interface, with one side embedded within a magnetic field, where there is a discontinuity in quantities such as density and temperature at this interface (Roberts 1981a). Next, two interfaces were considered, modeled by the "magnetic slab," where the external quantities to the waveguide are the same on the two sides. This highly popular and applicable configuration was investigated in both a nonmagnetic (Roberts 1981b) and a magnetic (Edwin & Roberts 1982) external environment. More recent work has been carried out considering the magnetic slab model, but now the equilibrium quantities on one side of the slab are different from those on the other side of the slab forming an asymmetric ambient plasma environment. This, of course, affects the waves that propagate, as, e.g., we see the different densities of the external environments directly affects the amplitudes of the perturbations, with the effect being dependent on which type of wave is propagating. This asymmetric waveguide system was studied with a nonmagnetic external region (Allcock & Erdélyi 2017) and with a magnetic external region (Zsámberger et al. 2018). Considering asymmetry is important when examining waveguides that have local inhomogeneity in their equilibrium quantities such as, e.g., the density. A few solar applications of the asymmetric magnetic slab configuration have been explored in, e.g., Allcock et al. (2019), where observations of waves in chromospheric fibrils, modeled as asymmetric slabs, are used to obtain estimates of the chromospheric Alfvén speed. A further example where density, magnetic, and flow asymmetry may be considered important is that of MBP's, as discussed in Zsámberger et al. (2018) and Allcock et al. (2019).

The purpose of the current investigation is to build on previous work on the magnetic slab embedded in an asymmetric nonmagnetic environment (Allcock & Erdélyi 2017), by considering now standing waves. To do this, a

line-tying boundary condition will be imposed, so that quantities such as the component of the velocity perturbation that is perpendicular to the slab walls, and the total pressure perturbation, are zero at the end points of the slab. In doing this, we expect reflection of the propagating waves from the ends of the slab to cause interference, which leads to the formation of standing waves. We also assume the thin slab and weak asymmetry approximations in order to make analytical progress. In this case, it will then be possible to analyze how the asymmetry and the properties of the slab (e.g., the thin width compared to the wavelength) affect both the eigenfrequencies and amplitudes of the standing waves.

The waves supported by a magnetic slab embedded in an asymmetric environment can be categorized into two types based on the motion that is observed. The "quasi-sausage" wave exhibits velocity perturbations at each interface in opposite directions. The "quasi-kink" wave exhibits velocity perturbations at each interface in the same direction. The quasi-sausage and quasi-kink waves are analogous to the sausage and kink waves introduced in the symmetric slab in Roberts (1981b), with some altered properties due to the asymmetry in the equilibrium parameters. The waves can be further categorized into two types based on the spatial distribution of the perturbation amplitudes. The term "surface modes" refers to the oscillations where the maximum amplitude of oscillation occurs on the boundaries of the slab, whereas the term "body modes" refers to the oscillations where the maximum amplitude of oscillation occurs somewhere inside the slab. This study will focus on surface modes, and the study of body modes is not included. The main reason for this is that our work is concerned with how the asymmetry affects the standing waves, and body modes are generally less sensitive to changes in the external environment (Allcock & Erdélyi 2017). In Roberts (1981b), the various propagating waves permitted in a magnetic slab are further categorized into slow and fast modes. However, only the slow modes can exist in the system we are considering, as the two types of fast modes that may appear in the symmetric slab of arbitrary size do not exist under the assumptions made here. More precisely, the fast sausage surface wave that exists in the symmetric system degenerates due to the external sound speeds being different on the two sides of the slab, in the case of the thin slab approximation (Allcock & Erdélyi 2017), and so a fast quasi-sausage mode does not need to be considered. In addition, the fast kink surface wave that can exist in the symmetric study does not exist in the thin slab limit, as it changes its nature from a surface mode to a body mode as we reduce the size of the slab when compared to the wavelength (Edwin & Roberts 1982). Introducing asymmetry will not enable the appearance of the fast quasi-kink mode in this limit, and therefore a fast quasi-kink mode does not need to be considered.

Joarder & Roberts (1992) conducted a study that included standing waves due to periodic boundary conditions in the context of prominences. However, the boundary conditions used in this study were not consistent, as their Equations (26) and (27) did not satisfy the assumption (Equation (25)) for certain values of n, m. Additionally, there is limited analytical detail provided regarding the standing waves. Our work provides a much more detailed analysis of standing MHD waves.

In what follows, first, we present the equilibrium of the system along with the appropriate line-tying boundary conditions in Section 2. Then, the equations governing the disturbances inside the slab, along with the dispersion relation, are derived in Section 3.1. This dispersion relation is formally identical to the one derived in Allcock & Erdélyi (2017). The thin slab and weak asymmetry assumptions are then applied to simplify the dispersion relation in Section 3.2. Section 4 is devoted to examining the eigenfrequencies of the standing harmonic modes, by deriving an analytic expression for the frequency and using this to investigate quantities that highlight how the width of the slab and the asymmetry affect the oscillations. A similar procedure is used in Section 5 to examine the amplitudes of the standing harmonic modes. Numerical solutions to the full dispersion relation are given in Section 6, followed by a discussion of the results in Section 7.

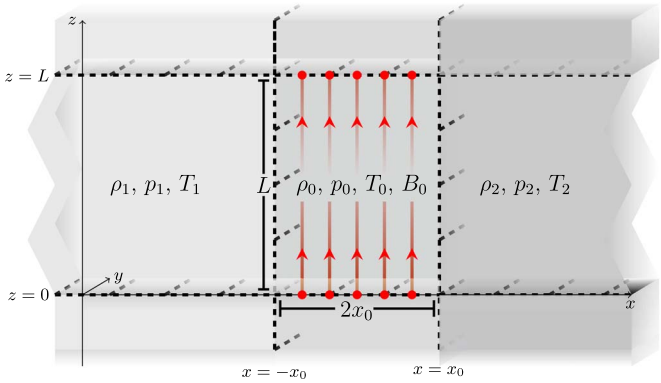

Figure 1. Equilibrium state inside ($|x| \leqslant x_0$) and outside of the magnetic slab ($x < -x_0$ and $x > x_0$). The red lines indicate the magnetic field. The slab is bounded by four dashed lines at $x = -x_0$, $x = x_0$, $z = 0$, and $z = L$.

2. The Equilibrium Magnetic Slab

Consider a three-dimensional, inviscid, static, ideal plasma split into three regions in the x-direction. This equilibrium configuration is shown in Figure 1. The middle region (or the "slab") has a width in the x-direction of $2x_0$, and a finite length of L in the z-direction (and is unbounded in the y-direction). There is also an equilibrium magnetic field given by $B(x)\hat{\boldsymbol{e}}_z$, where

$$B(x) = B_0 \quad \text{if } |x| \leqslant x_0, \tag{1}$$

$$B(x) = 0 \quad \text{if } |x| > x_0, \tag{2}$$

where B_0 is constant. The equilibrium kinetic plasma pressure, temperature, and density are denoted p_i, T_i, and ρ_i, respectively, for $i = 0$ inside the slab, $i = 1$ on the left of the slab, and $i = 2$ on the right of the slab. Throughout this work, the effects of gravity are ignored. As this work aims to analyze the effect of asymmetry on standing waves, and we do not wish to examine magnetoacoustic gravity waves, this simplification is justified.

2.1. Boundary Conditions

There are boundary conditions that must be applied at the interfaces, $x = \pm x_0$, and at the end points of the slab, $z = 0, L$.

We must have pressure balance across the interfaces at $x = \pm x_0$ in order for the equilibrium to be stable:

$$p_1 = p_0 + \frac{B_0^2}{2\mu_0} = p_2, \tag{3}$$

where μ_0 is the permeability of free space. Sound speeds are denoted by $c_i = \sqrt{\frac{\gamma p_i}{\rho_i}}$ for $i = 0, 1, 2$, where γ is the adiabatic index, which is taken to be constant across the entire system, under the assumption that the plasma composition is the same throughout. We will denote the Alfvén speed inside the slab by $v_A = \frac{B_0}{\sqrt{\rho_0 \mu_0}}$. Equation (3) gives a useful relationship between the external sound speeds and densities:

$$c_1^2 \rho_1 = c_2^2 \rho_2. \tag{4}$$

The assumption of line-tying gives us boundary conditions that we must apply at $z = 0, L$. The conditions that are relevant to our study are that the x-component of the velocity perturbation, v_x, and the z-component of the magnetic field perturbation, b_z, are zero at $z = 0, L$. Additionally, by defining the total pressure perturbation p_T to be the sum of the kinetic plasma pressure perturbation and the magnetic pressure perturbation, we can impose that the total pressure perturbation is also zero at $z = 0, L$. Mathematically, these conditions correspond to

$$v_x(z=0) = v_x(z=L) = 0, \quad b_z(z=0) = b_z(z=L) = 0, \times p_T(z=0) = p_T(z=L) = 0. \tag{5}$$

3. Derivation of the Dispersion Relation

In order to analytically examine both the frequencies and amplitudes of eigenoscillations in the slab system given in Figure 1, the linear governing equations for disturbances must be derived. This, along with the boundary conditions determined above (see Equation (5)), will then be used to derive the dispersion relation, and then simplifications will be made using the thin slab and weak asymmetry assumptions.

3.1. The General Dispersion Relation

In this section, the dispersion relation governing the linear waves in a magnetic slab will be derived, before any additional simplifications are made. A similar derivation is given to that in Allcock & Erdélyi (2017); however, there are some important differences due to the line-tying boundary condition.

3.1.1. The Ideal MHD Equations

To derive the linear governing equation for the disturbances inside the slab, we must start with the ideal MHD equations:

$$\rho \frac{D\boldsymbol{v}}{Dt} = -\nabla p - \frac{1}{\mu_0}\boldsymbol{B} \times (\nabla \times \boldsymbol{B}), \tag{6}$$

$$\frac{\partial \rho}{\partial t} + \nabla.(\rho \boldsymbol{v}) = 0, \tag{7}$$

$$\frac{D}{Dt}\left(\frac{p}{\rho^\gamma}\right) = 0, \tag{8}$$

$$\frac{\partial \boldsymbol{B}}{\partial t} = \nabla \times (\boldsymbol{v} \times \boldsymbol{B}) [\text{along with the constraint } \nabla.\boldsymbol{B} = 0], \tag{9}$$

where ρ, p, $\boldsymbol{B}$, and $\boldsymbol{v}$ are the density, pressure, magnetic field, and velocity, respectively.

Linearization about the basic state ρ_0, p_0, $\boldsymbol{B}_0(=B_0\boldsymbol{e_z})$, and $\boldsymbol{v}_0(=0)$, where ρ_0, p_0, B_0, are constant, gives equations for the perturbations ρ', p', $\boldsymbol{b} = (b_x, b_y, b_z)$, and $\boldsymbol{v} = (v_x, v_y, v_z)$, of the density, pressure, magnetic field, and velocity, respectively. We also assume $v_y = 0$, and all quantities are independent of y, giving two coupled equations in v_x and v_z:

$$\frac{\partial^2 v_x}{\partial t^2} = c_0^2 \frac{\partial}{\partial x}(\nabla.\boldsymbol{v}) + v_A^2 \nabla^2 v_x, \tag{10}$$

$$\frac{\partial^2 v_z}{\partial t^2} = c_0^2 \frac{\partial}{\partial z}(\nabla.\boldsymbol{v}). \tag{11}$$

Equations (10) and (11) govern the disturbances inside the slab, and to proceed further we must apply the boundary conditions.

3.1.2. Boundary Conditions

To satisfy the line-tying boundary condition given by Equation (5), we assume

$$v_x = \hat{v}_x(x) e^{-i\omega t} \sin(kz), \quad v_z = \hat{v}_z(x) e^{-i\omega t} f(z), \quad p_T = \hat{p}_T(x) e^{-i\omega t} \sin(kz), \tag{12}$$

where f is an arbitrary function to be determined. When the line-tying boundary conditions are imposed, meaning $v_x(z=0) = v_x(z=L) = 0$, we obtain a condition on k:

$$k = \frac{n\pi}{L}, \quad n \in \mathbb{Z}^+, \tag{13}$$

where $k = 0$ is excluded to ensure we consider nontrivial solutions. Using Equations (10)–(12), we obtain that $f(z) = Q\cos(kz)$, for an arbitrary constant Q. The constant Q can be absorbed into, say, $\hat{v}_z(x)$, meaning we can take $f(z) = \cos(kz)$.

3.1.3. The Governing Equations

Substituting the expressions for v_x and v_z given by Equation (12) into Equations (10) and (11) gives

$$\frac{d^2\hat{v}_x}{dx^2} - m_0^2 \hat{v}_x = 0, \quad \text{where} \quad m_0^2 = \frac{(k^2c_0^2 - \omega^2)(k^2v_A^2 - \omega^2)}{(k^2c_T^2 - \omega^2)(c_0^2 + v_A^2)}, \quad c_T^2 = \frac{c_0^2 v_A^2}{c_0^2 + v_A^2}. \tag{14}$$

This governing ordinary differential equation is the same as Equation (11) in Allcock & Erdélyi (2017), and Equation (22) in Roberts (1981a), with $l = 0$.

Equation (14) is valid inside the slab, whereas we see that outside the slab we have

$$\frac{d^2\hat{v}_x}{dx^2} - m_i^2 \hat{v}_x = 0, \quad \text{where} \quad m_i^2 = k^2 - \frac{\omega^2}{c_i^2}, \quad \text{for} \quad i = 1, 2. \tag{15}$$

3.1.4. The Dispersion Relation

Using Equations (14) and (15) it is straightforward to write down the solution for $\hat{v}_x$ for all x. Using this, it is possible to calculate the total pressure, p_T, and apply the continuity of p_T and v_x across both $x = \pm x_0$. In doing so, it is possible to derive the dispersion relation for waves in an asymmetric slab embedded in a nonmagnetic environment (with the details

given in Allcock & Erdélyi 2017):

$$\omega^4 m_0^2 + \frac{\rho_0}{\rho_1} m_1 \frac{\rho_0}{\rho_2} m_2 (k^2 v_A^2 - \omega^2)^2 - \frac{1}{2} m_0 \omega^2 (k^2 v_A^2 - \omega^2) \left(\frac{\rho_0}{\rho_1} m_1 + \frac{\rho_0}{\rho_2} m_2 \right) \times (\tanh(m_0 x_0) + \coth(m_0 x_0) = 0. \quad (16)$$

If the asymmetry is removed (taking $\rho_1 = \rho_2$), after some algebra, it is possible to recover Equation (10) in Roberts (1981b), the dispersion relation for MHD waves in the magnetic slab embedded in a nonmagnetic symmetric environment.

3.2. Reduction in the Case of Weak Asymmetry and Thin Slab Approximations

This section will be focused on simplifying the dispersion relation using the thin slab and weak asymmetry assumptions. In the following, we will take $m_0^2 > 0$, to examine the surface modes of the system. We introduce the notation

$$\varepsilon = \frac{x_0}{L}, \quad \text{and} \quad \rho_2 = \rho_1 (1 + \delta), \quad \text{where} \quad \delta = \frac{\rho_2 - \rho_1}{\rho_1} > 0, \quad (17)$$

meaning we have taken $\rho_1 < \rho_2$ (without loss of generality).

3.2.1. The Weak Asymmetry Approximation

The weak asymmetry assumption corresponds to $\delta \ll 1$, and we can use this to simplify Equation (16). The dispersion relation to leading order in δ is then

$$(k^2 v_A^2 - \omega^2) \left(\frac{\rho_0}{\rho_1} m_1 + \frac{\rho_0}{\rho_2} m_2 \right) \approx 2\omega^2 m_0 \begin{pmatrix} \tanh \\ \coth \end{pmatrix} (m_0 x_0), \quad (18)$$

where δ is not explicitly written; however, it is included within both ρ_2 and m_2. Explicitly using δ (recall Equations (4) and (15)) gives

$$(k^2 v_A^2 - \omega^2) \frac{\rho_0}{\rho_1} m_1 \left(2 - \delta \left[1 + \frac{\omega^2}{2(k^2 c_1^2 - \omega^2)} \right] \right) \approx 2\omega^2 m_0 \begin{pmatrix} \tanh \\ \coth \end{pmatrix} (m_0 x_0). \quad (19)$$

Equation (18) is the same as that given in Equation (22) in Allcock & Erdélyi (2017). If we again compare Equation (18) to its counterpart for the slab in the symmetric environment, we see that the "tanh" term would correspond to sausage modes and the "coth" term would correspond to kink modes (Roberts 1981b). The terminology introduced in Allcock & Erdélyi (2017) will be employed here. More precisely, in Equation (18) the "tanh" term corresponds to quasi-sausage and the "coth" term to quasi-kink modes. The quasi-sausage and quasi-kink modes exhibit similar behavior to the usual sausage and kink modes; however, there will be important differences that enable us to carry out solar magnetoseismology diagnostics of an asymmetric waveguide system. This includes the amplitudes of oscillation, which will be different on each side of the slab (more of these differences are discussed in Allcock & Erdélyi 2017). Although this approach allows us to isolate the quasi-sausage and quasi-kink modes, not much analytical progress can be made without further simplification.

3.2.2. The Thin Slab Approximation

The thin slab approximation corresponds to $\varepsilon \ll 1$, and we can use this to simplify the dispersion relation Equation (16), by keeping only the leading terms in ε. Due to the line-tying boundary condition and Equation (13), $kx_0 = n\pi\varepsilon$, meaning that kx_0 is also a small quantity, and can be treated in the same way as ε. The dispersion relation then becomes

$$\omega^4 m_0^3 L\varepsilon + m_0 L\varepsilon \frac{\rho_0}{\rho_1} m_1 \frac{\rho_0}{\rho_2} m_2 (k^2 v_A^2 - \omega^2)^2 - \frac{1}{2} m_0 \omega^2 (k^2 v_A^2 - \omega^2) \left(\frac{\rho_0}{\rho_1} m_1 + \frac{\rho_0}{\rho_2} m_2 \right) \approx 0. \quad (20)$$

Numerical solutions given in Allcock & Erdélyi (2017) suggest that there is a slow quasi-sausage surface wave such that $\omega^2 \approx k^2 c_T^2$, and so by assuming the form $\omega^2 \approx k^2 c_T^2 (1 - \alpha\varepsilon)$, we see that, the angular frequency of the standing wave harmonics to leading order in ε is

$$\omega_n^2 \approx \frac{n^2 \pi^2 c_T^2}{L^2} \left[1 - \varepsilon \frac{2n\pi c_0^4 c_1 \rho_1}{\rho_0 (c_0^2 + v_A^2)^2} \times \left(\frac{1 + \delta}{(1 + \delta)(c_1^2 - c_T^2)^{\frac{1}{2}} + (c_1^2 - c_T^2 (1 + \delta)^{\frac{1}{2}}} \right) \right], \quad (21)$$

where we have used $k = \frac{n\pi}{L}$.

Numerical solutions given in Allcock & Erdélyi (2017) also suggest that there is a slow quasi-kink surface wave such that $\omega^2 \to 0$, as $\varepsilon \to 0$, and so by assuming the form $\omega^2 \approx \beta\varepsilon$, we see that, the angular frequency of the standing wave harmonics to leading order in ε is

$$\omega_n^2 \approx \varepsilon \frac{\rho_0 n^3 \pi^3 v_A^2}{L^2 \rho_1 (1 + \delta/2)}, \quad (22)$$

where again we have used $k = \frac{n\pi}{L}$.

Plots of the phase speed (ω_n/k) of the fundamental mode and the first harmonic, for both a range of ε and a range of δ, are given in Figures 2–5. The values for the parameters used in these plots (e.g., the sound speed) are chosen simply to illustrate the dependence on ε and δ. The values used would be different in the context of a prominence. In particular, the external sound speeds would be higher than the internal sound speed, and the internal density would be at least 10 times higher than the external densities (Priest 2014, p.57). However, these changes do not have a dominant effect on the general behavior of slow surface modes, which is what we focus on. While the corresponding pairs of wavenumber and phase speed values would be altered under the conditions frequently found in prominences, the existence of the slow surface modes is unchanged. Moreover, the general shape of their dispersion curves remains qualitatively the same, too: in the long wavelength limit, that the phase speed of the slow surface quasi-sausage mode still approaches the tube speed, while that of the quasi-kink mode still tends to zero. In the short wavelength (large ε) limit, the exact solutions for the two modes still tend to two distinct phase speed values due to the

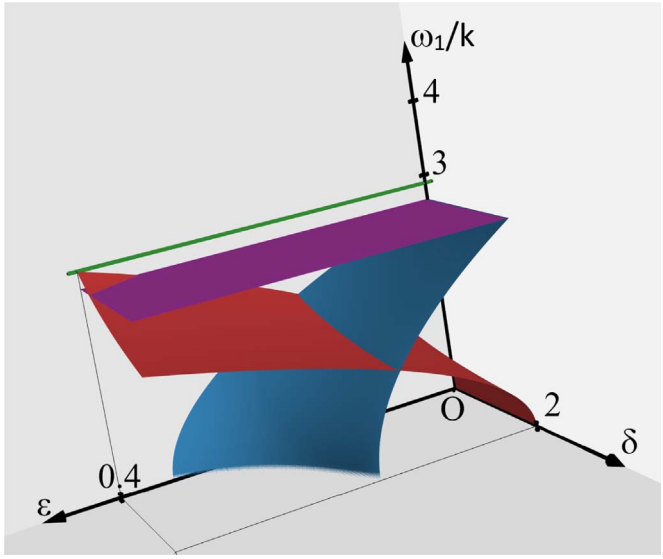

Figure 2. Phase speed for the fundamental mode ($n = 1$) as a function of ε ranging from 0 to 0.4, and δ ranging from 0 to 2. The blue surface is the quasi-sausage wave (given by Equation (21)), while the red surface is the quasi-kink waves (given by Equation (22)). The purple plane represents the value of c_T, and the green line illustrates the maximum plotted value, $\omega_1/k \approx 2.89$, by joining it to the vertical axis. The relevant values used for this plot are $c_0 = 5.00$, $v_A = 3.16$, $c_T = 2.67$, $c_1 = 4.71$, and $\rho_1/\rho_0 = 1.50$. Rotating animations of the 3D plot are available online.

(An animation of this figure is available.)

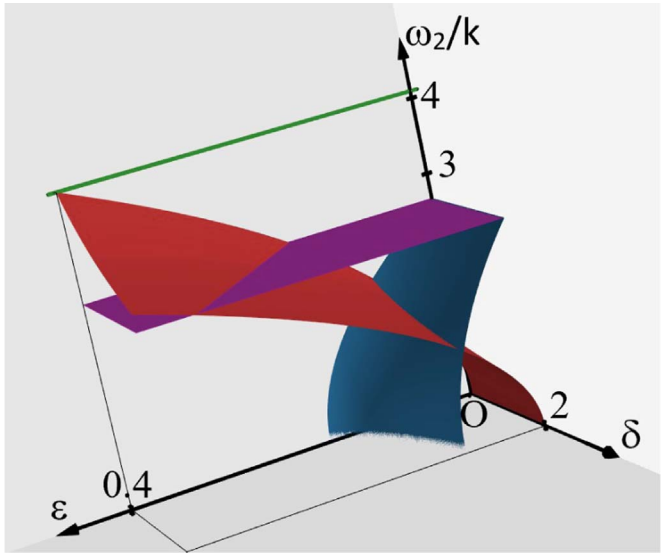

Figure 3. Same as in Figure 2 but for the first harmonic ($n = 2$), and the maximum plotted value is $\omega_2/k \approx 4.09$.

(An animation of this figure is available.)

presence of asymmetry, while the approximate solutions still intersect one another (which will be further discussed later).

In these plots, we have the restriction that ε be small (by assumption), but we have taken a large range of δ. Some combinations of ε and δ produce an expression with $\omega^2 < 0$, resulting in cutoffs in the plots for those values. Numerical solutions in Allcock & Erdélyi (2017) show that the eigenfrequencies, when plotted against the width of the slab, should not intersect. However, Figure 4 shows an intersection between $\varepsilon = 0.05$ and $\varepsilon = 0.1$ (for $\delta = 1$), suggesting that there is a restriction on the size of ε (valid ranges of ε and δ,

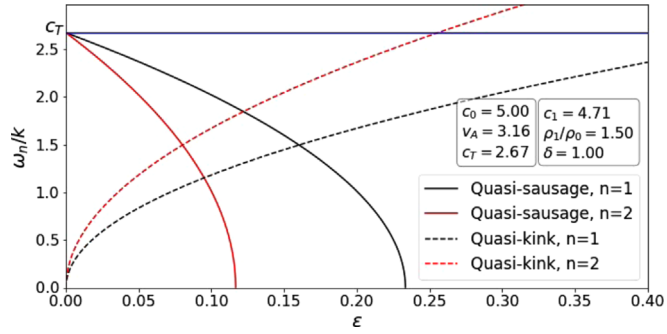

Figure 4. Phase speed for the fundamental mode ($n = 1$) and the first harmonic ($n = 2$) of the quasi-sausage waves (given by Equation (21)) and the quasi-kink waves (given by Equation (22)), as a function of ε ranging from 0 to 0.4, with $\delta = 1$ fixed. The other relevant quantities are given in the figure. The horizontal blue line represents the value of c_T.

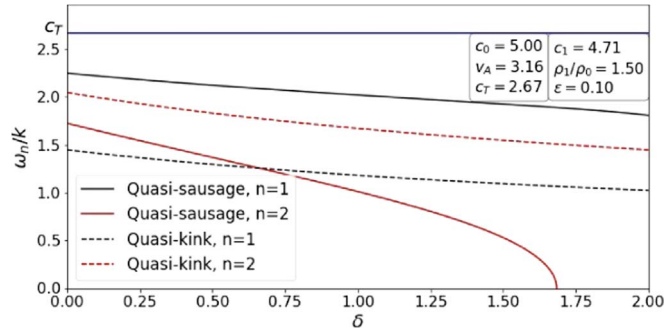

Figure 5. Same as in Figure 4, but the phase speed is plotted as a function of δ ranging from 0 to 2, with $\varepsilon = 0.1$ fixed.

under certain limits, will be discussed in Section 6). In accordance with Equation (21), Figure 4 also shows that, for a fixed value of δ, the phase speeds of the quasi-sausage modes decrease when the slab width is increased; while that of quasi-kink modes increases (as expected from Equation (22)). An interesting consequence of the form of these equations is, however, that due to the cubic dependence on the harmonic mode number (n), the phase speeds of the first harmonic of both kinds of modes change faster than those of the fundamental modes, resulting in the intersection occurring at thinner slab widths.

Similarly, Figure 5 illustrates the behavior of the eigenmodes for a fixed slab width. It is clear from this diagram that the phase speeds of the quasi-kink modes are less sensitive to differences in the asymmetry parameter than that of the quasi-sausage modes. This is especially noticeable for the first harmonic of the quasi-sausage mode, whose phase speed drops down to zero within the small range of δ plotted here. Lastly, Figures 2 and 3 provide a generalization of the phase speeds for various combinations of ε and δ.

The increased sensitivity of the first harmonics to changes in the measure of asymmetry or the width of the slab, compared to the fundamental modes, is confirmed for all these possible choices of parameters.

3.2.3. Ordering of ε and δ

In order to proceed further analytically, it will be assumed that we have both the thin slab and weak asymmetry approximations in place. Mathematically, this corresponds to $\varepsilon \ll 1$ and $\delta \ll 1$. This will mean that the leading order terms in both ε and δ can be identified. Let us also assume that the

higher the order in the small quantities ε and δ is, the smaller the size of the term becomes. More precisely, take $\varepsilon, \delta \gg \varepsilon^2, \varepsilon\delta, \delta^2$. In the following, we use Equation (18) to derive the frequencies and amplitudes of the standing modes analytically. In the derivation of Equation (18) we have ignored terms that contain a factor of δ^2, and are considered negligible. All subsequent calculations that use Equation (18) must therefore not include terms that would be affected by keeping these small terms. After the desired expressions are calculated, the additional ordering $\delta \ll \varepsilon$ will be taken simply to order the terms by size, and some visualization will then be presented showing our results for a range of ε and δ. Note that in the plots, some regions better approximate the solutions to the full dispersion relation than others, due to the relative sizes chosen for ε and δ.

4. Frequencies of the Standing Harmonic Modes

The focus in this section is to derive the eigenfrequencies of the system analytically, and use this to determine quantities that highlight how the asymmetry will affect the oscillations. We study the frequency as it is a popular quantity to measure, and we aim to identify how sensitive the eigenfrequencies are to changes in the external environment.

Equation (18) (the simplified dispersion relation) will be examined separately for the quasi-sausage and quasi-kink modes. As well as calculating the eigenfrequencies, we will determine the ratio of the first harmonic to the fundamental mode, and the relative frequency difference due to the asymmetry. All three of these quantities can be compared with the corresponding counterpart where the system is symmetric, and this will highlight how asymmetry affects the oscillation. In particular, the frequency ratio is a measurable quantity so it would be suggested to compare the theory developed here with observational data once the required resolution is available. The relative difference due to asymmetry must be a small quantity, as this quantity would reduce to zero in the case of symmetry.

Another reason for calculating the relative frequency difference, is to compare the result we arrive at to the result for the relative amplitude difference due to asymmetry (in Section 5). By considering asymmetry as a *perturbation* to the symmetric slab model, we would expect to see that the relative frequency difference due to asymmetry (eigenfrequencies) has a higher order sensitivity to the perturbation than the relative amplitude difference due to asymmetry (eigenfunctions; see the Appendix).

4.1. Quasi-sausage Modes

4.1.1. Eigenfrequencies in the Thin Slab and Weak Asymmetry Approximations

Using Equation (18) along with the limit $\varepsilon \ll 1$, the dispersion relation for the quasi-sausage modes becomes

$$(k^2v_A^2 - \omega^2)\left(\frac{\rho_0}{\rho_1}m_1 + \frac{\rho_0}{\rho_2}m_2\right) \approx 2\omega^2 m_0^2 x_0\left(1 - \frac{m_0^2 x_0^2}{3}\right). \tag{23}$$

The most simple solution of Equation (23) is $\omega = kv_A$, but we will ignore this case. This solution would mean $m_0^2 = 0$, and using this in Equation (14) along with the requirement that the solution is evanescent, would give a trivial solution. Using

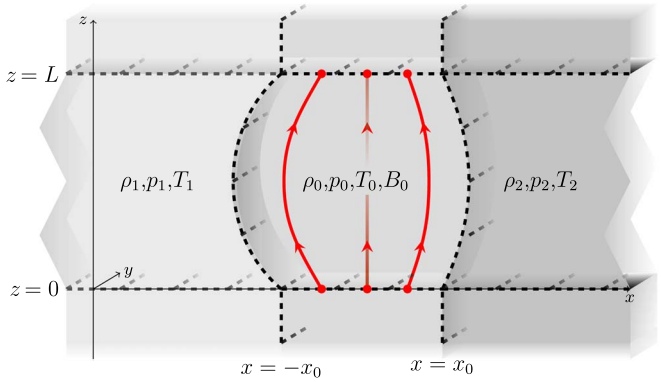

Figure 6. Illustration of a fundamental standing quasi-sausage mode oscillation in the asymmetric magnetic slab.

Equation (14), canceling a factor of $(k^2v_A^2 - \omega^2)$ and substituting in $\varepsilon = \frac{x_0}{L}$ leads to

$$\frac{\rho_0}{\rho_1}m_1 + \frac{\rho_0}{\rho_2}m_2 \approx 2\omega^2 \times \frac{(k^2c_0^2 - \omega^2)}{(k^2c_T^2 - \omega^2)(c_0^2 + v_A^2)}L\varepsilon\left(1 - \frac{m_0^2L^2\varepsilon^2}{3}\right). \tag{24}$$

If we introduce the notation

$$\Pi = \frac{c_0^4 c_1 \rho_1}{\rho_0(c_1^2 - c_T^2)^{\frac{1}{2}}(c_0^2 + v_A^2)^2}, \tag{25}$$

then there is a solution of Equation (24) given by the following (where we recall $k = \frac{n\pi}{L}$ due to the line-tying condition (Equation (13))):

$$\omega_n^2 \approx \frac{n^2\pi^2c_T^2}{L^2}\left[1 - \varepsilon n\pi\Pi - \varepsilon^2n^2\pi^2\left[\frac{\Pi^2(c_0^2 + v_A^2)}{2c_0^4(c_1^2 - c_T^2)} \times (4c_T^2c_1^2 - 3c_T^4 + c_0^2c_T^2 - 2c_0^2c_1^2) - \frac{c_T^2}{3(c_0^2 + v_A^2)}\right] - \varepsilon\delta\frac{n\pi\Pi(2c_1^2 - c_T^2)}{4(c_1^2 - c_T^2)}\right]. \tag{26}$$

Equation (26) gives the frequency of the slow quasi-sausage mode in the case of the thin slab and weak asymmetry. This expression gives the eigenfrequency as approximately $k^2c_T^2$ as expected, with terms due to the approximations. The leading correction term is of order ε, and there is no factor of δ until second order in the small quantities.

An illustration of both the fundamental mode and the first harmonic for the standing quasi-sausage wave solution is given in Figures 6 and 7. A diagram of the phase speed of the fundamental mode and the first harmonic, for both a range of ε and a range of δ, are given in Figures 8 and 9. The quasi-sausage and quasi-kink modes are plotted in the same figure.

Figure 8 shows the quadratic dependence of the phase speed on the parameter ε. It is also evident that as ε is taken smaller and smaller, the quasi-sausage and quasi-kink solutions are tending toward roughly the tube speed and zero respectively. As expected, Figure 9 shows that the phase speed does not change much as δ is changed. This is a consequence of the ranges chosen, but also a consequence of δ not appearing until second order in the small quantities.

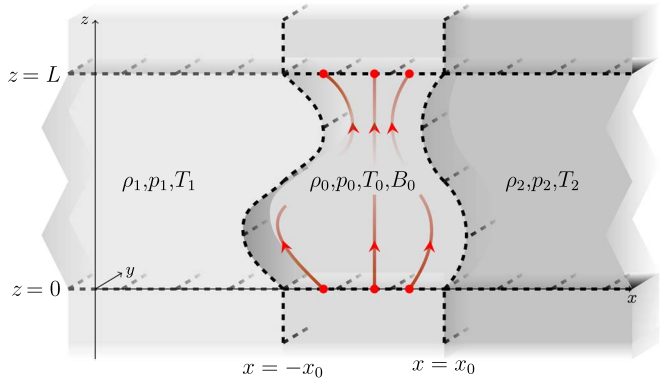

Figure 7. Same as Figure 6 but for the first harmonic.

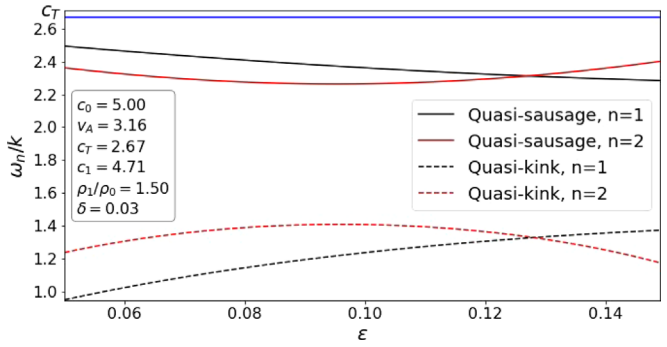

Figure 8. Phase speed for the fundamental mode ($n = 1$) and the first harmonic ($n = 2$) of the quasi-sausage waves (given by Equation (26)) and the quasi-kink waves (given by Equation (31)), as a function of ε ranging from 0.05 to 0.15, with $\delta = 0.03$ fixed. The other relevant quantities are given in the figure, and the horizontal blue line represents the value of c_T.

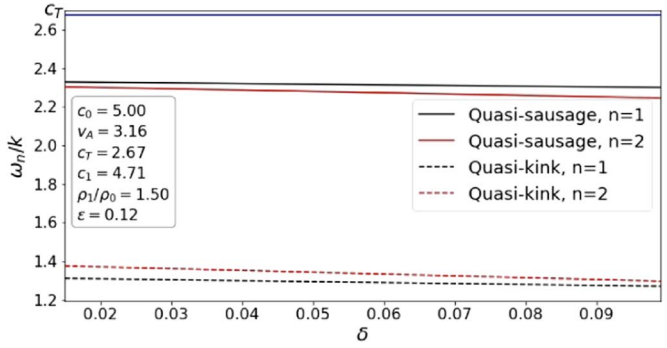

Figure 9. Same as in Figure 8, but the phase speed is plotted as a function of δ ranging from 0.015 to 0.1, with $\varepsilon = 0.12$ fixed.

4.1.2. Frequency Ratio of the First Harmonic to the Fundamental Mode

We can use Equation (26) to write the frequency ratio of the first harmonic to the fundamental mode as

$$\frac{\omega_2}{\omega_1} \approx 2\Bigg[1 - \varepsilon\frac{\pi\Pi}{2} - \varepsilon^2\pi^2\Bigg[\frac{\Pi^2(c_0^2 + v_A^2)}{8(c_1^2 - c_T^2)c_0^4}(19c_T^2c_1^2 - 13c_T^4 + c_0^2c_T^2 - 7c_0^2c_1^2) - \frac{c_T^2}{2(c_0^2 + v_A^2)}\Bigg] - \varepsilon\delta\frac{\pi\Pi(2c_1^2 - c_T^2)}{8(c_1^2 - c_T^2)}\Bigg]. \tag{27}$$

Plots of the frequency ratio of the first harmonic to the fundamental mode, for both a range of ε and a range of δ, are given in Figures 10 and 11. The quasi-sausage and quasi-kink modes are plotted in the same figure. Figure 10 shows that within this range of ε, the quasi-kink frequency ratio has a more sensitive dependence on ε than the quasi-sausage frequency ratio. Figure 11 illustrates that the quasi-kink mode has no dependence on δ up to the order of terms we have included, whereas the quasi-sausage mode has a linear relationship with δ.

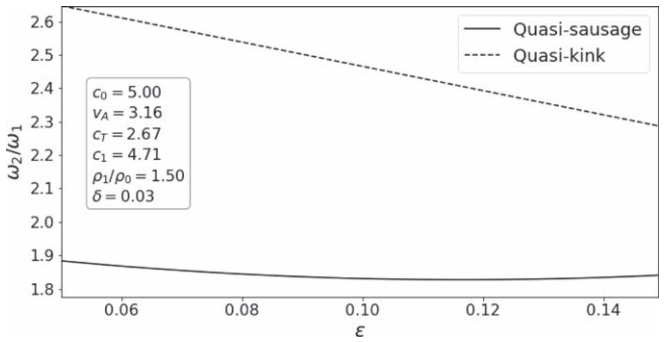

Figure 10. Ratio of the frequencies of the first harmonic to the fundamental mode of the quasi-sausage waves (given by Equation (27)) and the quasi-kink waves (given by Equation (32)), as a function of ε ranging from 0.05 to 0.15, with $\delta = 0.03$ fixed. The other relevant quantities are given in the figure.

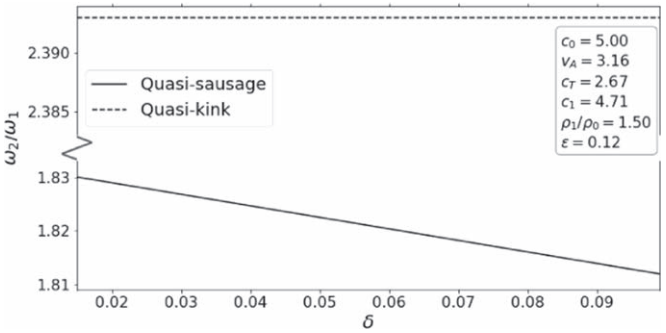

Figure 11. Same as in Figure 10, but the ratio is plotted as a function of δ ranging from 0.015 to 0.1, with $\varepsilon = 0.12$ fixed.

4.1.3. Relative Frequency Difference Due To Asymmetry

We introduce $\omega_{n,a}$ and $\omega_{n,s}$ which correspond to the eigenfrequencies of the mode n in the asymmetric and symmetric cases, respectively. Using Equation (26) gives us $\omega_{n,a}^2$ directly, and substituting in $\delta = 0$ gives $\omega_{n,s}^2$. Using Taylor expansions, we arrive at an equation for the relative change in frequency due to the asymmetry, which, for the quasi-sausage waves, is denoted $d_{\omega,S}$:

$$d_{\omega,S} = \left|\frac{\omega_{n,a} - \omega_{n,s}}{\omega_{n,s}}\right| \approx \varepsilon\delta\frac{n\pi\Pi(2c_1^2 - c_T^2)}{8(c_1^2 - c_T^2)}. \tag{28}$$

A plot of the frequency difference due to asymmetry, for both a range of ε and a range of δ, is given in Figures 12 and 13. The quasi-sausage and quasi-kink modes are plotted in the same figure. Figure 12 shows that the frequency difference for the quasi-kink modes does not depend on ε, whereas the quasi-sausage modes show a linear dependence on ε, with an increase in the slope as we move up through the modes (increasing n). Figure 13 shows that both the quasi-sausage and quasi-kink modes have a linear dependence on δ. For the quasi-sausage modes, we again see that as we move up through the modes,

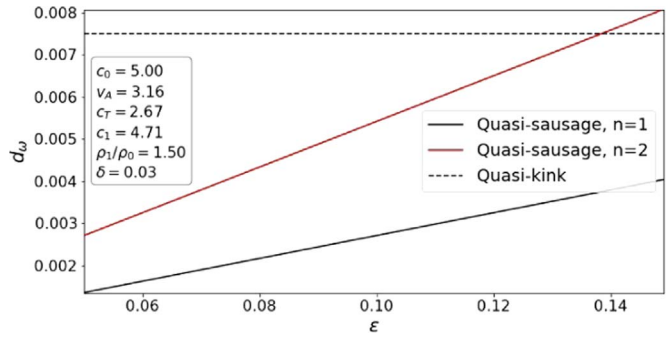

Figure 12. Frequency difference due to asymmetry of the fundamental mode ($n = 1$) and the first harmonic ($n = 2$) quasi-sausage waves (given by Equation (28)) and the quasi-kink waves (given by Equation (33)), as a function of ε ranging from 0.05 to 0.15, with $\delta = 0.03$ fixed. The other relevant quantities are given in the figure. The frequency difference due to asymmetry for the quasi-kink modes does not depend on n, giving only one curve, whereas $n = 1, 2$ is plotted for the quasi-sausage modes.

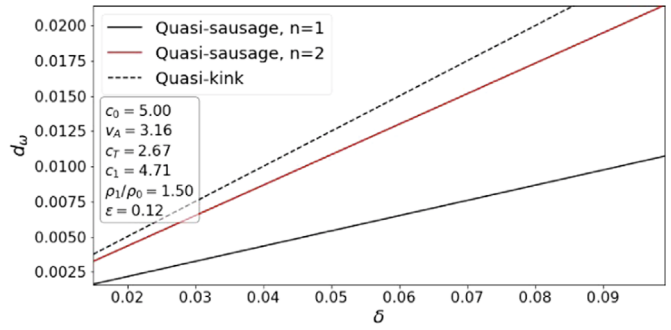

Figure 13. Same as in Figure 12, but the frequency difference is plotted as a function of δ ranging from 0.015 to 0.1, with $\varepsilon = 0.12$ fixed.

the slope of the curves is increased. Conversely, the frequency difference for the quasi-kink modes shows the same linear dependence on δ, regardless of which standing harmonic we take.

4.2. Quasi-kink Modes

4.2.1. Eigenfrequencies in the Thin Slab and Weak Asymmetry Approximations

Using Equation (18) along with the limit $\varepsilon \ll 1$, the dispersion relation for the quasi-kink modes is

$$(k^2 v_A^2 - \omega^2)\left(\frac{\rho_0}{\rho_1} m_1 + \frac{\rho_0}{\rho_2} m_2\right) \approx 2\frac{\omega^2}{x_0}. \tag{29}$$

Substituting in $\varepsilon = \dfrac{x_0}{L}$ and rearranging we arrive at

$$L\varepsilon(k^2 v_A^2 - \omega^2)\left(\frac{\rho_0}{\rho_1} m_1 + \frac{\rho_0}{\rho_2} m_2\right) \approx 2\omega^2. \tag{30}$$

There is a solution to Equation (30) given by (where we recall $k = \dfrac{n\pi}{L}$ due to the line-tying condition (Equation (13))):

$$\omega_n^2 \approx \varepsilon \frac{\rho_0 n^3 \pi^3 v_A^2}{2L^2 \rho_1}\left(2 - (n\pi\varepsilon)\frac{\rho_0}{\rho_1}\left(2 + \frac{v_A^2}{c_1^2}\right) - \delta\right). \tag{31}$$

Equation (31) gives the frequency of the slow quasi-kink mode in the limit of the thin slab and weak asymmetry. This eigenfrequency tends toward zero as the slab becomes more thin, as the entire expression contains a factor of ε. Note that there is no factor of δ up to second order in the small quantities. An illustration of both the fundamental mode and the first harmonic for the standing quasi-kink wave is given in Figures 14 and 15. Plots of the phase speeds corresponding to the frequencies given in Equation (31) are provided in Figures 8 and 9, with a small discussion provided where they were introduced in Section 4.1

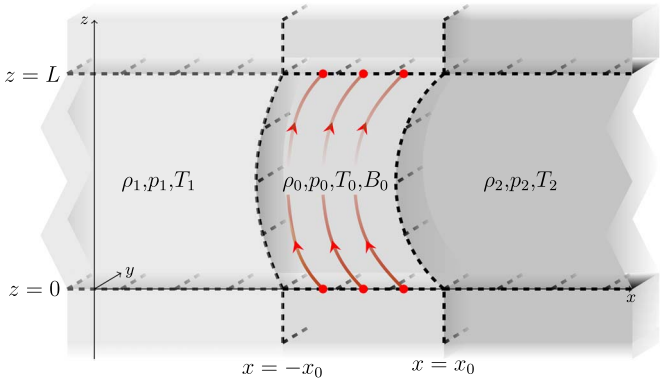

Figure 14. Illustration of a fundamental standing quasi-kink mode oscillation in the asymmetric magnetic slab.

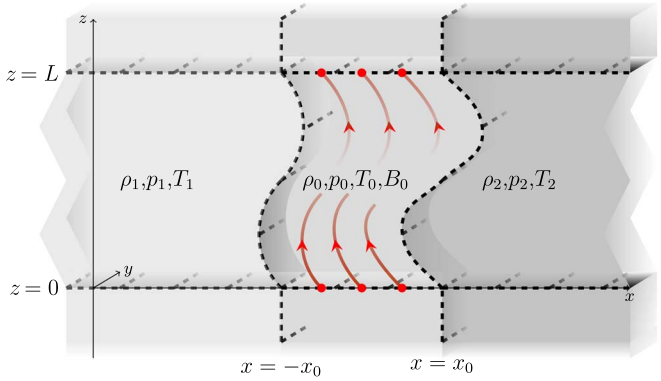

Figure 15. Same as Figure 14 but for the first harmonic.

4.2.2. Frequency Ratio of the First Harmonic to the Fundamental Mode

We can use Equation (31) to write the frequency ratio of the first harmonic to the fundamental mode as

$$\frac{\omega_2}{\omega_1} \approx 2\sqrt{2}\left(1 - \varepsilon\frac{\pi\rho_0}{4\rho_1}\left(2 + \frac{v_A^2}{c_1^2}\right)\right). \tag{32}$$

Only first order small terms have been included, as to keep second order small terms here, we would have to keep higher order terms in ω_n^2. Plots of the frequency ratio are given in Figures 10 and 11, with a small discussion provided where they were introduced in Section 4.1

4.2.3. Relative Frequency Difference Due To Asymmetry

Again, we introduce $\omega_{n,a}$ and $\omega_{n,s}$ which correspond to the frequency in the asymmetric and symmetric cases, respectively. Using Equation (31) gives us $\omega_{n,a}^2$ directly, and substituting in $\delta = 0$ gives $\omega_{n,s}^2$. Using Taylor expansions, we arrive at an equation highlighting the relative change in frequency due to

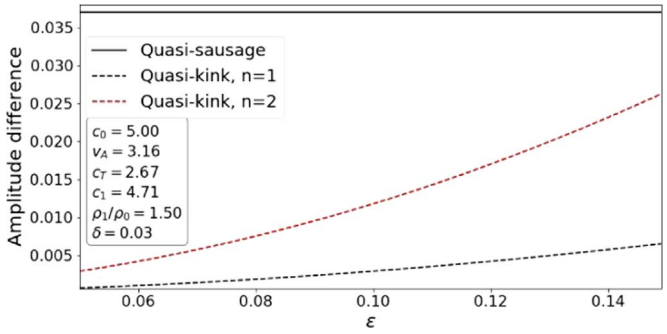

Figure 16. Amplitude difference between the two sides of the slab for the quasi-sausage waves (given by Equation (36)) and both the fundamental mode ($n = 1$) and the first harmonic ($n = 2$) quasi-kink waves (given by Equation (42)), as a function of ε ranging from 0.05 to 0.15, with $\delta = 0.03$ fixed. The other relevant quantities are given in the figure. The amplitude difference between the two sides of the slab for the quasi-sausage modes does not depend on n, giving only one curve, whereas $n = 1,2$ is plotted for the quasi-kink modes.

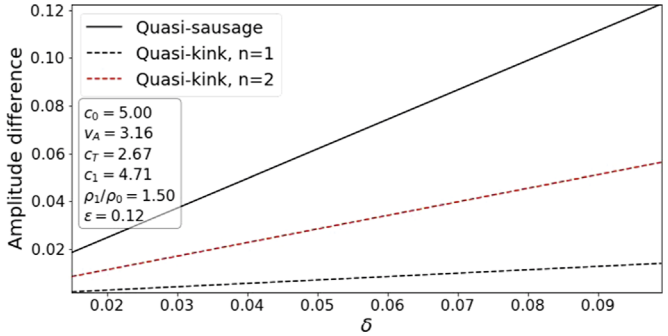

Figure 17. Same as in Figure 16, but the amplitude difference is plotted as a function of δ ranging from 0.015 to 0.1, with $\varepsilon = 0.12$ fixed.

the asymmetry, which, for the quasi-kink waves, is denoted $d_{\omega,K}$:

$$d_{\omega,K} = \left| \frac{\omega_{n,a} - \omega_{n,s}}{\omega_{n,s}} \right| \approx \frac{\delta}{4}. \tag{33}$$

We only keep the first order small terms here for the same reasons as applied to Equation (32). Plots of the frequency difference due to asymmetry are given in Figures 12 and 13, with a small discussion provided where they were introduced in Section 4.1

5. Amplitudes of the Standing Harmonic Modes

The amplitude of the eigenoscillations can be examined to give useful information about the standing harmonic modes, and how the asymmetry and the small width of the slab affect them. The following quantities will be considered. First, the relative difference in amplitude between the two sides of the slab will be calculated by taking the difference in amplitude between one side of the slab and the other, and then dividing this by the amplitude on one side in order to give us a dimensionless quantity. We denote this quantity by $R_{S,1}$ for the quasi-sausage and $R_{K,1}$ for the quasi-kink modes. We introduce these quantities as they are expected to reduce to zero in the case of a symmetric slab, so it will be useful to examine how they depend on δ. In addition to this, the amplitudes of the oscillations are measurable in theory, so the possibility of using SMS techniques to infer background quantities gives us motivation to study them. Second, the relative amplitude difference compared to the symmetric slab will be calculated by taking the difference between the maximum amplitude of the oscillation in the asymmetric case and the symmetric case, then dividing by the symmetric case. We denote this quantity by $R_{S,2}$ for the quasi-sausage and $R_{K,2}$ for the quasi-kink modes, respectively. This second quantity is introduced for a similar reason as the first quantity was. In addition to this, it can be used to compare with the relative frequency difference due to asymmetry as described in the introduction to Section 4. In this section, the relevant quantities are calculated to leading order in the small quantities ε and δ.

We introduce the notation $\hat{v}_{x,a}$ for the velocity perturbation in the asymmetric case, and $\hat{v}_{x,s}$ for the velocity perturbation in the symmetric case. We will use $\hat{\xi}_x(x) = i\hat{v}_x(x)/\omega$, which gives the amplitude of displacement perturbation when we have a static background equilibrium, and we define $\hat{\xi}_{x,a}$ and $\hat{\xi}_{x,s}$ analogously to the velocity perturbations.

5.1. Quasi-sausage Modes

5.1.1. Relative Amplitude Difference between the Two Sides of the Slab

For the quasi-sausage modes, $\hat{v}_x(x_0)$ and $\hat{v}_x(-x_0)$ (as well as $\hat{\xi}_x(x_0)$ and $\hat{\xi}_x(-x_0)$) will have opposite signs, so the quantity we are interested in is

$$R_{S,1} = \left| \frac{\hat{\xi}_x(x_0) + \hat{\xi}_x(-x_0)}{\hat{\xi}_x(-x_0)} \right| = \left| \frac{\hat{v}_x(x_0) + \hat{v}_x(-x_0)}{\hat{v}_x(-x_0)} \right|. \tag{34}$$

It is then possible to derive the following expression:

$$R_{S,1} = \left| \frac{m_0\omega^2(\rho_2 m_1 - \rho_1 m_2)}{m_0 m_1 \omega^2 \rho_2 + \rho_0 m_2 m_1(\omega^2 - k^2 v_A^2)\tanh(m_0 x_0)} \right|. \tag{35}$$

Using Taylor expansions and the eigenfrequency given by Equation (26), we find

$$R_{S,1} \approx \delta \frac{2c_1^2 - c_T^2}{2(c_1^2 - c_T^2)}. \tag{36}$$

The relative amplitude difference between the two sides of the slab is shown as a function of ε and δ in Figures 16 and 17. The quasi-sausage and quasi-kink modes are plotted in the same figure. Figure 16 shows that the quasi-sausage amplitude difference between the two sides of the slab does not depend on ε, while the quasi-kink amplitude difference between the two sides of the slab displays a quadratic curve. On the other hand, Figure 17 shows that for both the quasi-sausage and quasi-kink modes, the amplitude difference between the two sides of the slab has a linear relationship with δ

Rearranging Equation (36), we can obtain an approximation for the Alfvén speed inside the slab as

$$v_A^2 \approx \frac{2(R_{S,1} - \delta)c_1^2 c_0^2}{c_0^2(2R_{S,1} - \delta) - 2c_1^2(R_{S,1} - \delta)}. \tag{37}$$

Expression (37) is useful, as the Alfvén speed is directly related to the magnetic field strength through the relation $v_A = \dfrac{B_0}{\sqrt{\rho_0 \mu_0}}$, and if we are able to obtain observed values of the quantity $R_{S,1}$, this result can then be used to determine an approximate value of the magnetic field strength B_0.

5.1.2. Relative Amplitude Difference Compared to the Symmetric Slab

The maximum amplitude for the quasi-sausage mode occurs on the side of the slab with smaller external density (Allcock & Erdélyi 2017), and as $\rho_1 < \rho_2$, this is at $x = -x_0$ (as shown in Figures 6 and 7). We can then write down an equation for $R_{S,2}$:

$$R_{S,2} = \left| \frac{\hat{\xi}_{x,a}(-x_0) - \hat{\xi}_{x,s}(-x_0)}{\hat{\xi}_{x,s}(-x_0)} \right| = \left| \frac{\hat{v}_{x,a}(-x_0) - \hat{v}_{x,s}(-x_0)}{\hat{v}_{x,s}(-x_0)} \right|. \quad (38)$$

It is then possible to derive the following expression:

$$R_{S,2} \approx \delta \frac{2c_1^2 - c_T^2}{4(c_1^2 - c_T^2)}. \quad (39)$$

A plot of the relative amplitude difference compared to the symmetric slab is not given, since, for both the quasi-sausage and quasi-kink, these are qualitatively the same as the relative amplitude difference between the two sides of the slab, with the only difference being a factor of two.

5.2. Quasi-kink Modes

5.2.1. Relative Amplitude Difference between the Two Sides of the Slab

For the quasi-kink modes, $\hat{v}_x(x_0)$ and $\hat{v}_x(-x_0)$ (as well as $\hat{\xi}_x(x_0)$ and $\hat{\xi}_x(-x_0)$) will have the same sign, so the quantity we are interested in is

$$R_{K,1} = \left| \frac{\hat{\xi}_x(x_0) - \hat{\xi}_x(-x_0)}{\hat{\xi}_x(-x_0)} \right| = \left| \frac{\hat{v}_x(x_0) - \hat{v}_x(-x_0)}{\hat{v}_x(-x_0)} \right|. \quad (40)$$

It is then possible to derive the following expression:

$$R_{K,1} = \left| \frac{m_0\omega^2(\rho_2 m_1 - \rho_1 m_2)\tanh(m_0 x_0)}{\rho_0 m_2 m_1 (k^2 v_A^2 - \omega^2) - \omega^2 \rho_2 m_1 m_0 \tanh(m_0 x_0)} \right|. \quad (41)$$

Using Taylor expansions, recalling $k = \frac{n\pi}{L}$ and $\varepsilon = \frac{x_0}{L}$ and using the frequency given by Equation (31), we find

$$R_{K,1} \approx \delta \varepsilon^2 n^2 \pi^2. \quad (42)$$

Plots of the relative amplitude difference between the two sides of the slab are given in Figures 16 and 17, with a small discussion provided where they were introduced in Section 5.1

5.2.2. Relative Amplitude Difference Compared to the Symmetric Slab

The maximum amplitude for the quasi-kink mode occurs on the side of the slab with larger external density (Allcock & Erdélyi 2017), and as $\rho_1 < \rho_2$, this is at $x = x_0$ (as shown in Figures 14 and 15). We can then write down an equation for $R_{K,2}$:

$$R_{K,2} = \left| \frac{\hat{\xi}_{x,a}(x_0) - \hat{\xi}_{x,s}(x_0)}{\hat{\xi}_{x,s}(x_0)} \right| = \left| \frac{\hat{v}_{x,a}(x_0) - \hat{v}_{x,s}(x_0)}{\hat{v}_{x,s}(x_0)} \right|. \quad (43)$$

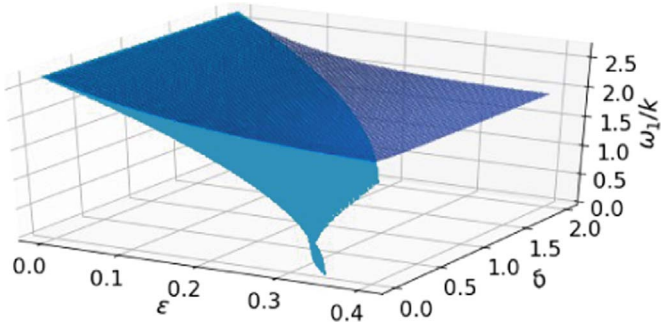

Figure 18. Phase speed for the fundamental mode ($n = 1$) of the quasi-sausage waves as a function of ε ranging from 0 to 0.4, and δ ranging from 0 to 2. The lighter blue colored (bottom) surface is plotted by using Equation (21), while the darker blue colored (top) surface is for using numerical methods to solve the asymmetric dispersion relation given by Equation (16). The relevant values used for this plot are $c_0 = 5.00$, $v_A = 3.16$, $c_T = 2.67$, $c_1 = 4.71$, and $\rho_1/\rho_0 = 1.50$.

(An animation of this figure is available.)

It is then possible to derive the following expression:

$$R_{K,2} \approx \delta \varepsilon^2 \frac{n^2\pi^2}{2}. \quad (44)$$

A plot of the relative amplitude difference compared to the symmetric slab is not given due to the similarities with Figures 16 and 17, as explained in Section 5.1.

6. Numerical Solutions of the Dispersion Relation

In this section, numerical methods are used to solve the full dispersion relation for standing waves in an asymmetric magnetic slab, given by Equation (16). These numerical solutions are then plotted on the same axes as plots created using the analytical solutions to the approximate dispersion relation for a thin slab, given by Equation (20). It will then be possible to demonstrate what values of the small parameter ε can be considered small enough for the analytical solutions to give accurate results, and the ranges of ε and δ used to illustrate results in Section 4 will be justified.

The phase speeds of the quasi-sausage and quasi-kink fundamental modes are plotted in Figures 18 and 19, respectively. For the quasi-sausage mode, the decreasing of either δ or ε decreases the size of the gap between the two surfaces. Consequently, if we take δ to be small, we are justified in taking larger ε values than if we take δ large. More precisely, if we aim to satisfy $\delta \ll \varepsilon$ (as we used for the illustrations in Section 4), we are justified in taking a combination of ε and δ where $0.01 < \delta < 0.1$ and ε is as large as $\varepsilon \approx 0.19$, as then the maximum percentage difference between the values of the two surfaces is approximately 20% (to calculate this, we take the difference between the values on the two surfaces, and divide by the value on the larger surface). For the quasi-kink mode, we see that decreasing δ increases the size of the gap between the two surfaces, whereas decreasing ε decreases the size of the gap between the two surfaces. If we again aim to satisfy $\delta \ll \varepsilon$, then taking the combination of ε and δ where $0.01 < \delta < 0.1$ and ε as large as $\varepsilon \approx 0.19$ is justified, as then the maximum percentage difference between the values of the two surfaces is approximately 20%. Therefore taking the ranges of ε and δ used in Section 4 for the illustrations ($0.01 < \delta < 0.1$ with $\varepsilon = 0.12$ and $0.05 < \varepsilon < 0.15$ with $\delta = 0.03$) are justified, and our analytical results provide

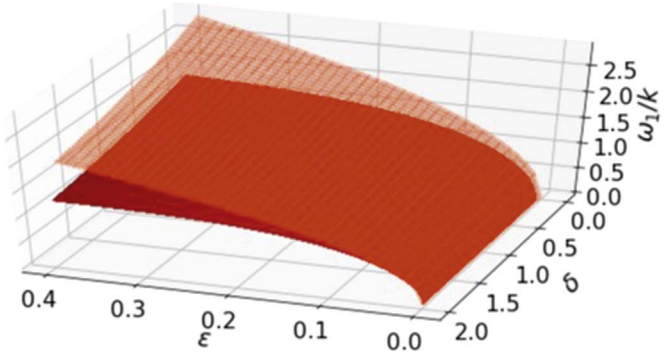

Figure 19. Same as in Figure 18 but for the quasi-kink wave. The light red (top) surface is created by using Equation (22), while the darker red (bottom) surface is created using numerical methods to solve the asymmetric dispersion relation given by Equation (16).

(An animation of this figure is available.)

good accuracy for these ranges. It should be noted that this calculation is only an example using the fundamental mode ($n = 1$). If the first harmonic ($n = 2$) were to be analyzed in a similar way, the percentage difference would be larger.

7. Discussion

Building on the symmetric slab model introduced by Roberts (1981b), along with the asymmetric slab model described by Allcock & Erdélyi (2017), standing modes in the asymmetric slab model have been studied, and their properties analyzed, in order to understand how the asymmetry affects both the amplitudes and the frequencies. In addition to this, by taking the thin slab approximation, it was possible to analyze how the width of the slab affects the standing harmonic modes. The results derived, first in the general case of a thin slab, with arbitrary asymmetry, suggest the frequency has a complex dependence on δ (given by Equations (21) and (22)).

In addition to this, from Figures 2 and 3, we see that the qualitative nature of the phase speed is very similar for each fixed ε, and each fixed δ.

Taking the weak asymmetry approximation enables us to examine analytically how the standing modes are affected by asymmetry (δ) to leading order. Sections 4 and 5 provide a mathematical description of this dependence. From both the Equations (26) and (31) and plots (Figures 8 and 9) provided, it is evident that under the approximations of a thin slab and weak asymmetry, the frequencies and phase speeds of the standing harmonic modes are much more sensitive to changes in the width of the slab, than to changes in the asymmetry of the system.

In the limit as the slab becomes infinitesimally small, we expect the slab to behave like a string with fixed ends, and then the frequency ratio should approach a value of $\omega_2/\omega_1 = 2$. This is what we observe for the quasi-sausage mode, taking $\varepsilon \to 0$ in Equation (27). For the quasi-kink mode, taking $\varepsilon \to 0$ in Equation (32), we see that $\omega_2/\omega_1 \to 2\sqrt{2}$. This is a direct consequence of the vanishing frequency for the quasi-kink mode as the width of the slab is reduced to zero. More precisely, as we take the limit $\varepsilon \to 0$, we see $\omega_n \to 0$, and we have no wave and hence no meaningful frequency ratio.

The frequency difference due to asymmetry, and the amplitude difference compared to the symmetric slab, were introduced as a way of making a comparison between the eigenfrequencies and the eigenfunctions of the system. By considering the asymmetry as a perturbation to the symmetric slab model, we expect the frequency difference due to asymmetry (eigenfrequencies) to have a higher order sensitivity when compared with the amplitude difference due to asymmetry (eigenfunctions; more details are given in the Appendix). For the quasi-sausage modes, using Equations (28) and (39) we see that this does occur as expected, with the frequency difference due to asymmetry proportional to $\varepsilon\delta$, and the amplitude difference due to asymmetry proportional to δ. However, the quasi-kink mode does not seem to obey this rule, as Equations (33) and (44) show that the frequency difference due to asymmetry is proportional to δ, and the amplitude difference due to asymmetry is proportional to $\varepsilon^2\delta$. This is a consequence of the factor of ε that is present in the frequency of the standing harmonic modes, meaning that there is no constant term and we cannot expect this result for the quasi-kink modes.

The authors acknowledge the support received from the SURE scheme at the University of Sheffield. N.Z. is also grateful to the School of Mathematics and Statistics at the University of Sheffield, and to the University of Debrecen. R.E. is also grateful to Science and Technology Facilities Council (STFC, grant No. ST/M000826/1) UK and the Royal Society for enabling this research. R.E. also acknowledges the support received by the CAS Presidents International Fellowship Initiative grant No. 2019VMA052 and the warm hospitality received at USTC of CAS, Hefei, where part of his contribution was made. The authors thank Mihai Barbulescu for the code used to solve the dispersion relation numerically (https://github.com/BarbulescuMihai/PyTES).

Appendix
The Rayleigh–Ritz Technique

Let $\boldsymbol{\xi}_i$, $i = 0, 1, 2, \ldots$ be the eigenvectors of the ideal linear MHD force operator, $\boldsymbol{F}\{\xi_i\}$, which therefore satisfy the equation $\boldsymbol{F}\{\boldsymbol{\xi}_i\} = -\rho_0\omega_i^2\boldsymbol{\xi}_i$. The eigenvalues ω_i^2, $i = 0, 1, 2, \ldots$ are ordered such that $\omega_0 < \omega_1 < \omega_2 \ldots$ i.e., ω_0 could be the sausage or kink eigenfrequency of a symmetric slab MHD waveguide.

If the eigenvector $\boldsymbol{\xi}_0$ is known, the corresponding eigenfrequency can be determined from the kinetic energy, K_0 and the change in potential energy, δW_0 of the system that results from the displacement $\boldsymbol{\xi}_0$ as

$$\omega_0^2 = \frac{\delta W_0\{\boldsymbol{\xi}_0^*, \boldsymbol{\xi}_0\}}{K_0\{\boldsymbol{\xi}_0^*, \boldsymbol{\xi}_0\}}, \tag{45}$$

where

$$K_0\{\boldsymbol{\xi}_0^*, \boldsymbol{\xi}_0\} = \frac{1}{2}\int \rho_0 \boldsymbol{\xi}_0^* \cdot \boldsymbol{\xi}_0 dV,$$

$$\delta W_0\{\boldsymbol{\xi}_0^*, \boldsymbol{\xi}_0\} = -\frac{1}{2}\int \boldsymbol{\xi}_0^* \cdot \boldsymbol{F}\{\boldsymbol{\xi}_0\} dV = \omega_0^2 K_0\{\boldsymbol{\xi}_0^*, \boldsymbol{\xi}_0\}, \tag{46}$$

and * denotes the complex conjugate (see also Equations (22.7), (22.21), and (25.12)–(25.16) in Schnack 2009).

Let us now perturb $\boldsymbol{\xi}_0$, by introducing a (weakly) asymmetric environment in the slab MHD waveguide resulting in a perturbed eigenvector $\boldsymbol{\xi}$. Then, we can write that

$$\boldsymbol{\xi} = \boldsymbol{\xi}_0 + \boldsymbol{\delta\xi}, \tag{47}$$

where $\boldsymbol{\delta\xi}$ is caused by the linear perturbation. By definition, the perturbation $\boldsymbol{\delta\xi}$ is orthogonal to (i.e., has no projection along)

the unperturbed eigenvector $\boldsymbol{\xi}_0$ (it contains all the parts of $\boldsymbol{\xi}$ that differ from $\boldsymbol{\xi}_0$), so that we can write

$$\boldsymbol{\xi} = \boldsymbol{\xi}_0 + \sum_{i=1}^{\infty} a_i \boldsymbol{\xi}_i, \tag{48}$$

where $i = 0$ has been excluded from the summation. We now want to estimate the perturbed eigenvalue, taking into account the energy contribution of the added asymmetry:

$$\omega^2 = \frac{\delta W\{\boldsymbol{\xi}_0^* + \boldsymbol{\delta\xi}^*, \boldsymbol{\xi}_0 + \boldsymbol{\delta\xi}\}}{K\{\boldsymbol{\xi}_0^* + \boldsymbol{\delta\xi}^*, \boldsymbol{\xi}_0 + \boldsymbol{\delta\xi}\}}. \tag{49}$$

We expand the new kinetic and potential energies corresponding to the perturbed state as

$$\begin{aligned}\delta W\{\boldsymbol{\xi}_0^* + \boldsymbol{\delta\xi}^*, \boldsymbol{\xi}_0 + \boldsymbol{\delta\xi}\} = \delta W\{\boldsymbol{\xi}_0^*, \boldsymbol{\xi}_0\} + \delta W\{\boldsymbol{\xi}_0^*, \boldsymbol{\delta\xi}\} \\ + \delta W\{\boldsymbol{\delta\xi}^*, \boldsymbol{\xi}_0\} + \delta W\{\boldsymbol{\delta\xi}^*, \boldsymbol{\delta\xi}\},\end{aligned} \tag{50}$$

and

$$\begin{aligned}K\{\boldsymbol{\xi}_0^* + \boldsymbol{\delta\xi}^*, \boldsymbol{\xi}_0 + \boldsymbol{\delta\xi}\} = K\{\boldsymbol{\xi}_0^*, \boldsymbol{\xi}_0\} + K\{\boldsymbol{\xi}_0^*, \boldsymbol{\delta\xi}\} \\ + K\{\boldsymbol{\delta\xi}^*, \boldsymbol{\xi}_0\} + K\{\boldsymbol{\delta\xi}^*, \boldsymbol{\delta\xi}\}.\end{aligned} \tag{51}$$

The second and third terms on the right-hand-side of Equation (50) are equal to one another due to the self-adjoint nature of $\boldsymbol{F}$, and equal to zero because of the orthogonality of the eigenvectors. Similar considerations can be made for Equation (51). Applying the definitions from Equations (46) to the rest of the terms, we obtain

$$\begin{aligned}\delta W\{\boldsymbol{\xi}_0^* + \boldsymbol{\delta\xi}^*, \boldsymbol{\xi}_0 + \boldsymbol{\delta\xi}\} = \delta W_0 + \frac{1}{2}\rho_0 \sum_{i=1}^{\infty} |a_i|^2 \omega_i^2, \\ K\{\boldsymbol{\xi}_0^* + \boldsymbol{\delta\xi}^*, \boldsymbol{\xi}_0 + \boldsymbol{\delta\xi}\} = K_0 + \frac{1}{2}\rho_0 \sum_{i=1}^{\infty} |a_i|^2,\end{aligned} \tag{52}$$

where, by Equations (46), $K_0 = \rho_0/2$.

Substituting these results into Equation (49), the denominator can be expanded if the perturbation to the system due to asymmetry ($\boldsymbol{\delta\xi}$) is small (for more details of this derivation, see Chapter 27 of Schnack 2009). Then, an estimate of the eigenvalue ω^2 as a result of linear perturbation is

$$\omega^2 \sim \omega_0^2 + \sum_{i=1}^{\infty} |a_i|^2 (\omega_i^2 - \omega_0^2), \tag{53}$$

where ω_0^2 is the actual eigenvalue (i.e., sausage or kink frequency) of the unperturbed (symmetric) system associated with $\boldsymbol{\xi}_0$. Here, the summation is the contribution to the eigenvalue of the unperturbed (symmetric) waveguide system caused by the introduction of asymmetry. The following properties can be observed:

(1) Even though the perturbation $\boldsymbol{\delta\xi}$ in our estimate of the eigenvector is $O(a_i)$ (see Equation (48)), the perturbation in the estimate of the eigenvalue is $O(|a_i|^2) << O(a_i)$. Therefore, the perturbation in the eigenvalue caused by the introduced asymmetry is much smaller than the perturbation in the eigenvector. As an example, say, a 10% linear perturbation introduced by asymmetry in the eigenvector $\boldsymbol{\xi}_0$ results in only a 1% perturbation in the estimate of the waveguides eigenfrequency ω^2.

(2) It is worth noting that the introduction of the waveguide asymmetry cannot result in an instability given that $\omega_0^2 < \omega_i^2$.

ORCID iDs

William Oxley https://orcid.org/0000-0001-7434-0292
Noémi Kinga Zsámberger https://orcid.org/0000-0002-2822-129X
Róbert Erdélyi https://orcid.org/0000-0003-3439-4127

References

Allcock, M., & Erdélyi, R. 2017, SoPh, 292, 35
Allcock, M., Shukhobodskaia, D., Zsámberger, N. K., & Erdélyi, R. 2019, FrASS, 6, 48
Andries, J., van Doorsselaere, T., Roberts, B., et al. 2009, SSRv, 149, 3
Arregui, I., Oliver, R., & Ballester, J. L. 2012, LRSP, 9, 2
Aschwanden, M. J., Fletcher, L., Schrijver, C. J., & Alexander, D. 1999, ApJ, 520, 880
Banerjee, D., Erdélyi, R., Oliver, R., & O'Shea, E. 2007, SoPh, 246, 3
DeForest, C. E., & Gurman, J. B. 1998, ApJL, 501, L217
de Moortel, I. 2009, SSRv, 149, 65
Edwin, P. M., & Roberts, B. 1982, SoPh, 76, 239
Erdélyi, R. 2006a, RSPTA, 364, 351
Erdélyi, R. 2006b, in ESA Special Publication 624, Proceedings of SOHO 18/GONG 2006/HELAS I, Beyond the Spherical Sun, ed. K. Fletcher (Noordwijk: ESA), 15
Erdélyi, R., & Taroyan, Y. 2008, A&A, 489, L49
Joarder, P. S., & Roberts, B. 1992, A&A, 256, 264
Keys, P. H., Morton, R. J., Jess, D. B., et al. 2018, ApJ, 857, 28
Liu, Y., Xiang, Y., Erdélyi, R., et al. 2018, ApJ, 856, 17
Nakariakov, V. M. 2006, RSPTA, 364, 473
Nakariakov, V. M., & Ofman, L. 2001, A&A, 372, L53
Nakariakov, V. M., & Verwichte, E. 2005, LRSP, 2, 3
Ofman, L., Romoli, M., Poletto, G., Noci, G., & Kohl, J. L. 1997, ApJL, 491, L111
Priest, E. 2014, Magnetohydrodynamics of the Sun (Cambridge: Cambridge Univ. Press)
Roberts, B. 1981a, SoPh, 69, 27
Roberts, B. 1981b, SoPh, 69, 39
Roberts, B., Edwin, P. M., & Benz, A. O. 1984, ApJ, 279, 857
Ruderman, M. S., & Erdélyi, R. 2009, SSRv, 149, 199
Schnack, D. 2009, Lectures in Magnetohydrodynamics (Berlin: Springer), 780
Tandberg-Hanssen, E. 1995, The Nature of Solar Prominences, Astrophysics and Space Science Library, Vol. 199 (Dordrecht: Kluwer)
Tsiropoula, G., Tziotziou, K., Kontogiannis, I., et al. 2012, SSRv, 169, 181
Uchida, Y. 1970, PASJ, 22, 341
Wang, T. J. 2004, in ESA Special Publication 547, SOHO 13 Waves, Oscillations and Small-Scale Transients Events in the Solar Atmosphere: Joint View from SOHO and TRACE, ed. H. Lacoste (Noorwijk: ESA), 417
Yang, S., Zhang, J., & Erdélyi, R. 2016, ApJL, 833, L18
Yang, S., Zhang, J., Erdélyi, R., et al. 2017, ApJL, 843, L15
Yuan, D., Nakariakov, V. M., Huang, Z., et al. 2014, ApJ, 792, 41
Zajtsev, V. V., & Stepanov, A. V. 1975, IGAFS, 37, 3
Zaqarashvili, T. V., & Erdélyi, R. 2009, SSRv, 149, 355
Zsámberger, N. K., Allcock, M., & Erdélyi, R. 2018, ApJ, 853, 136